Annals of Mathematics and Computer Science ISSN: 2789-7206
Vol 22 (2024) 12-44 https://doi.org/10.56947/amcs.v22.275

MACHINE LEARNING IMPACT OF RADIATIVE BLOOD FLOW OVER A WEDGE IN A TIME-DEPENDENT MHD WILLIAMSON FLUID

P. PRIYADHARSHINIR[1]* AND V. KARPAGAM[2]

Abstract. The main objective of this research is to examine the radiation effects of an unsteady MHD Williamson bio-fluid(Blood) over a wedge that interacts with thermophoresis diffusion and Brownian motion. The necessary prerequisites of partial differential equations (PDEs) ensure the development of suitable mathematical frameworks for momentum, energy, and concentration. These appropriate nonlinear PDEs are frequently transmuted into ordinary differential equations (ODEs) by implemented similarity transformation. The results of these ODEs have a significant impact on the BVP4C approach from the MATLAB package computational structures. The graphs and tabular data provided the various values for pertinent parameters on the non-dimensional velocity temperature, concentration profiles, and the numerical values of skin friction, Nusselt number, and Sherwood number were found and discussed in detail. A novel aspect of the research effort was the effective incorporation of multiple linear regression (MLR) employing machine learning (ML), a statistical technique to forecast the physical quantities for present numerical results with an accuracy of 95%. Finally, the response and predicted variables were verified using linear regression. The potential benefit of these outcomes is to develop novel therapeutic and diagnostic strategies for cancer treatment, as well as for a better understanding of medical problems and designing more effective drug delivery systems. In particular, for significant developments in computer technology and resources, the enormous computational cost of these simulations still keeps them from becoming a clinical tool. An additional benefit is that the outcomes showed acceptable congruence with the tangible findings of recent research and enlargements for future investigators.

1. Introduction and preliminaries

The current investigation explored the radiation effects of an unstable MHD Williamson fluid blood flow over a wedge despite being affected by the thermophoresis diffusion and Brownian motion. The impact of radiation on blood flow has bio-medical implications for many different therapeutic modalities. Recent studies support the effectiveness of heat therapy in reducing muscle spasms,

Date: Received: Feb 7, 2024; Accepted: Mar 1, 2024.
* Corresponding author.
2020 *Mathematics Subject Classification.* Primary 82D10, 76W05, 62J05, 80A21.
Key words and phrases. Blood flow, Machine Learning, Magneto Hydrodynamics, Multiple Linear Regression, Thermal radiation.

myalgia (muscle pain), fibromyalgia, and irreversible muscle shortening (called contracture in medicine). The majority of clinical studies, including those executed by et al. ([1]–[3]), examined that ultrasonic and infrared radiation affects blood flow. In addition to the advantages of radiation heat transfer in blood vessels already discussed, medical experts are especially concerned about the radiation effect on blood when treating hyperthermia, which has a well-established impact on oncology. Misra et al. [4] discovered theoretical estimates of blood flow in arteries during the therapeutic procedure of electromagnetic hyperthermia utilized in cancer treatment to kill fast-growing cancer cells.

Mandal et al. [5] addressed an unstable study of the non-Newtonian blood flow in tapered arteries under stenosis. Unsteady flow and mass mobility in fluid-structure interaction-based stenotic artery simulations studied by Valencia et al. [6]. The impact of the applied magnetic field on blood flow velocity resistance in a fictitious stenotic artery because wall shear stress enhances to a considerable extent for steeper stenosis looked into Bali et al. [7]. The concentration of magnetic nano-particles in biofluid (blood) under the influence of a high-gradient magnetic field is represented numerically explored by Habibi et al. [8]. The flow of blood via a tapering artery about stenosis impacted by heat transfer and chemical interactions constructed for N S Akbar et al. [9]. Blood flow in a permeability-sloping stretched visco-elastic dissipation, non-uniform heat source/sink, and chemical reactions executed by S R R Reddy et al. [10].

The evaluations of heat transfer and flow past wedge-shaped entities sparked a great deal of interest in both the engineering and chemical industries. Groundwater pollution, packed bed reactors, geothermal energy, oil recovery, and aerodynamics are real-world utilizations for this fluid. This concept was initially suggested by Falkner et al. [11]. Several differential techniques are applied to solve the governing partial differential equations numerically. The literature on physical processes has various references to the Falkner-Skan flow results. By incorporating viscous dissipation as a variable in the energy equation, B L Kuo et al. [12] established the convective flow of non-Newtonian Sisko liquid. The effects of thermal radiation on MHD-driven convection flow near a non-isothermal wedge with a heat source or sink analyzed by Chamkha et al. [13]. K L Hsiao et al. [14] reviewed MHD mixed convection for Visco-elastic fluid past a porous wedge. The flow of a micro-polar fluid through a porous wedge containing radiative surface boundaries that follow unstable hydro-magnetic forced convective heat transmission inspected M S Alam et al. [15].

Williamson et al. [16] specified the experiment results of non-Newtonian pseudo-plastic materials. In this model, the effective viscosity should continuously drop as the shear rate increases. Implementation of pseudo-plastic boundary layers of Williamson fluids employed in the industrial sector consists of higher molecular weight polymer compounds, emulsion-coated polymer sheets used in extrusion, and photographic films. S Sreenadh et al. [17] evaluated the impact of slip and heat transfer on the peristaltic pumping of an investigation into Williamson fluid in an inclined channel. C S Raju et al. [18] created the relationship between the temperature of a heat source and the Casson and Williamson fluid flow on a stretched sheet of materials. The effects of thermophoresis and the Brownian moment on the parabolic flow of magnetically-driven Casson and Williamson fluids with cross-diffusion assessed by G Kumaran et al. [19]. O D Makinde et al. [20] investigated the effects of thermal radiation and heat source/sink on the boundary-layer flow of nanofluids through a nonlinear stretching sheet when thermodynamic magnetism was applied.

C H Amanulla et al. [21] observed the effects of slip on the flow of an MHD Williamson fluid via a vertical convective boundary employed numerical computation. Ahmed et al. [22] determined Magnetohydrodynamic Williamson nanofluid flow past a rapidly rising barrier. The development of innovative computational models for thermal conductivity and temperature-dependent viscosity-driven stable MHD convective flows of radiative Casson fluids across a horizontally extended sheet in unstable geometry searched by Wakif et al. [23]. The numerical analysis of bio-convective nanofluid on a magnetohydrodynamic slip flow with step-blowing achieved by Tuz et al. [24]. Basha et al. [25] constructed Blood nanofluid flow for gyrotactic bacteria with three distinct geometries for numerical models.

The current research remarkable performance expectations provided for the previously suggested successful outcomes by B L Kuo et al. [26], Ishaq et al. [27], and Aamir Hamid et al. [28]. K Subbarayudu et al. [29] examined the influence of blood flow in a wedge using the unsteady Williamson fluid as the current investigation. From the literature review, the Williamson fluid model for unsteady flows under radiation affects blood flow along a wedge. The preceding experiment revealed that the Hartmann number raised for higher velocity, and the Weissenberg number developed for lower velocity. The temperature profile enhanced for the thermophoresis diffusion, Brownian motion, and radiation parameters all increased.

The four parts of this ongoing endeavor are the flow analysis, solution methodology, results and discussion, and conclusion. The present research study explored the effects of thermophoresis and Brownian motion on blood flow radiating over a wedge in a Williamson fluid. The MATLAB software BVP4C solver has been utilized in the above experiment to establish a feasible numerical approach for solving these equations under boundary conditions sufficient to the empirical circumstance. The unique feature of the present study is the application of a multiple linear regression analysis that was enhanced using a machine learning technique to predict the accuracy of the outcomes and minimize the error. Further analysis of this investigation implemented the linear regression technique to validate the numerical and anticipated results. Finally, a conclusion of the numerical and machine learning findings demonstrated excellent evidence of earlier results. The present work focused on flow and heat transport in capillary blood, with possible applications in clinical sciences, particularly thermal treatment for cancer cells.

2. Flow Analysis

A two-dimensional unstable and viscous wedge-shaped MHD Williamson fluid model with a consequence of Brownian motion and the thermophoresis effect.

The streatching velocity is assumed to be $u_w(x,t) = \frac{bx^m}{1-ct}$. Here, b stands for the stretching rate, and c represents a constant getting a dimension $(time)^{-1}$. An upward flow along the wedge axis described by a free stream velocity of $u_e(x,t) = \frac{ax^m}{1-ct}$, where the positive constants are a, c, and m. The range of m is $0 \leqslant m \leqslant 1$. The wedge angle of the fluid must be $\Omega = \beta\pi$, where $\beta = \frac{2m}{m+1}$ is related to the temperature gradient. It should be absorbing capacity, releasing ability, and the grey shade, but not distributing capability. A continuous magnetic field is perpendicular to the wedge. The cross-sectional applied magnetic field, the applied magnetic field, the external electric field, the charge polarization-related electric field, and the magnetic Reynolds number are all tiny.

The wedge surface is affected by the external magnetic field, which is applied regularly and has the formula $B(t) = \frac{B_0}{\sqrt{(1-ct)}}$. The stretching geometry serves as the x-axis alignment in the Cartesian coordinate system utilized for this study, with the y-axis often pointing outward from it. In our examination of heat transport, the initial variables used were temperature and concentration at the wedge's surface. $T_w(x,t) = T_\infty + \frac{T_0 x u_w}{\nu\sqrt{(1-ct)}}$, and $C_w(x,t) = C_\infty + \frac{C_0 x u_w}{\nu\sqrt{(1-ct)}}$ The beginning values of T_0 and C_0 indicate the temperature and concentration. When y approached infinity, the free stream obtained the constant values T_∞ and C_∞. Assuming electric fields are absent coming from the outside and a boundary layer. The visual representation and geometric structure of the physical model under investigation are demonstrated in Figure 1. Figure 2 depicted the flowchart of the recommended technique in a streamlined format to highlight the relevant details.

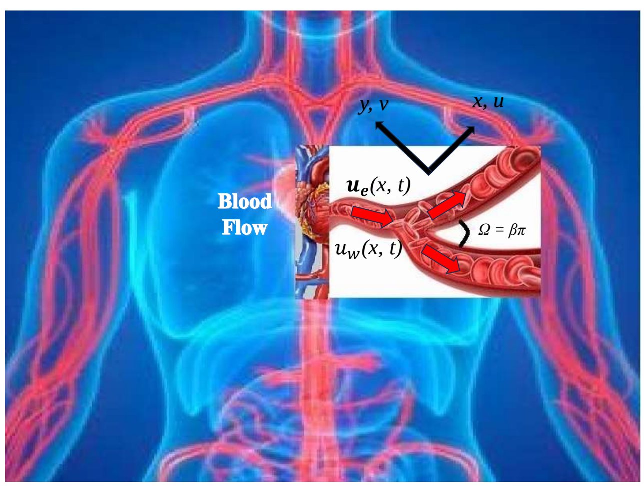

Figure 1. Proposed Geometrical diagram

The mathematical frameworks of governing equations on the continuity, momentum, energy, and concentration equations that were derived by et al. ([29], [30], [31], [32]).

$$u_x + v_y = 0, \tag{2.1}$$

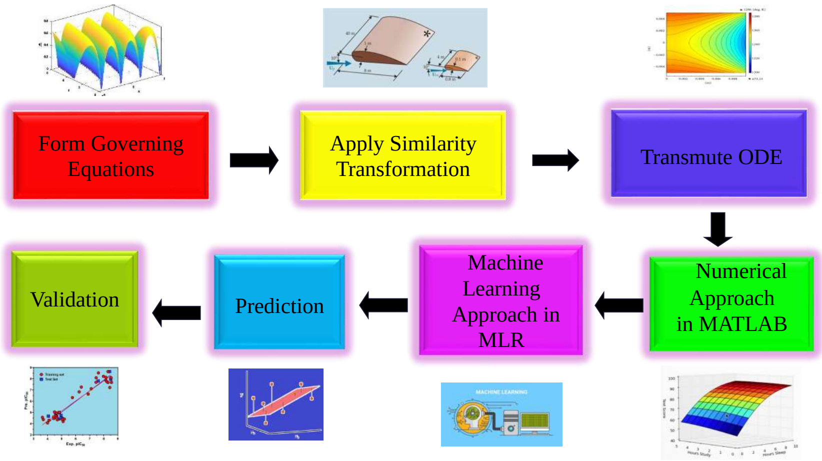

FIGURE 2. Flow Chart of Proposed Approach

$$\begin{aligned} u_t + uu_x + vu_y = u_{e_t} + u_e u_{e_x} + \nu u_{yy}\left[\beta^* + (1-\beta^*)(1-\Gamma u_y)^{-1}\right] + \\ \nu\Gamma u_y u_{yy}\left[(1-\beta^*)(1-\Gamma u_y)^{-2}\right] - \frac{\sigma B^2(t)}{\rho}(u-u_e), \end{aligned} \tag{2.2}$$

It is significant to note that the governing partial differential Eq. (2.2) of Williamson fluid flow reduced to the viscous fluid case when $\beta^* = 0 = \Gamma$.

$$T_t + uT_x + vT_y = \alpha T_{yy} - \frac{1}{(\rho c)_f} q_{r_y} + \tau\left[D_B C_y T_y + \frac{D_T}{T_\infty}(T_y)^2\right], \tag{2.3}$$

The radiative heat flow q_r is given after applying the Rosseland approximation for visually thick fluid. Now introducing, $q_r = -\frac{4\sigma^*}{3k^*}T_y^4$,

With the help of the Taylor series, the nonlinear component T^4 can be linearized while retaining terms up to first order only by accounting for a little difference between the fluid temperature inside the boundary layer and the atmospheric fluid temperature. T^4 value represented as follows: $T^4 \approxeq 4T_\infty^3 T - 3T_\infty^4$,

After substituting T^4 value in q_r the updated energy Eq. (2.3) is given by

$$T_t + uT_x + vT_y = \alpha T_{yy} + \frac{16\sigma^* T_\infty^3}{3\rho C_P k_1^*} T_{yy} + \tau\left[D_B C_y T_y + \frac{D_T}{T_\infty}(T_y)^2\right], \tag{2.4}$$

$$C_t + uC_x + vC_y = D_B C_{yy} + \frac{D_T}{T_\infty} T_{yy}. \tag{2.5}$$

The boundary conditions are as follows:

$$\begin{aligned} u = u_w, v = 0, T = T_w(x,t), C = C_w(x,t) \ at \ y = 0, \\ u \to u_e, T \to T_\infty, C \to C_\infty \ as \ y \to \infty. \end{aligned} \tag{2.6}$$

Utilized the following non-dimensional quantities et al. [33] to build the flow model without dimensions:

$$\eta = y\sqrt{\frac{(m+1)u_e}{2\nu x}}, \psi = \sqrt{\frac{2\nu x u_e}{(m+1)}} f(\eta), \theta(\eta) = \frac{T - T_\infty}{T_w - T_\infty}, \phi(\eta) = \frac{C - C_\infty}{C_w - C_\infty}. \tag{2.7}$$

Thus, the continuity Eq. (2.1) is identically satisfied by the stream function $\psi(x, y, t)$. Then, we get the velocity components from $u = \psi_y, v = -\psi_x$, respectively. We obtained the corresponding nonlinear ordinary differential conditions by replacing the non-dimensional parameters described in Eqs. (2.2), (2.4), and (2.5):

$$\begin{aligned}\left[\beta^* + (1-\beta^*)\left(1 - Wef''(\eta)\right)^{-2}\right] f'''(\eta) + f(\eta)f''(\eta) + \beta\left(1 - [f'(\eta)]^2\right) - \\ A(2-\beta)\left(f'(\eta) + \frac{\eta}{2}f''(\eta) - 1\right) - Ha^2(2-\beta)\left(f'(\eta) - 1\right) = 0,\end{aligned} \tag{2.8}$$

$$\begin{aligned}\frac{1}{Pr}\left(1 + \frac{4}{3}Rd\right)\theta''(\eta) + \left(f(\eta)\theta'(\eta) - 2f'(\eta)\theta(\eta)\right) - \frac{A}{2}(2-\beta)\left(\eta\theta'(\eta) + 3\theta(\eta)\right) + \\ Nb\theta'(\eta)\phi'(\eta) + Nt[\theta'(\eta)]^2 = 0,\end{aligned} \tag{2.9}$$

$$\begin{aligned}\frac{1}{Le}\left(\phi''(\eta) + \frac{Nt}{Nb}\theta''(\eta)\right) - \frac{A}{2}(2-\beta)\left(\eta\phi'(\eta) + 3\phi(\eta)\right) - \\ 2f'(\eta)\phi(\eta) + f(\eta)\phi'(\eta) = 0.\end{aligned} \tag{2.10}$$

The transformed boundary constraints are,

$$\begin{aligned} f(0) = 0, f'(0) = \lambda, \theta(0) = 1, \phi(0) = 1, \ at\ \eta = 0, \\ f'(\infty) \to 1, \theta(\infty) \to 0, \phi(\infty) \to 0, \ as\ \eta \to \infty. \end{aligned} \tag{2.11}$$

$\lambda = \frac{b}{a}$ is the wedge moving parameter. Stretching wedges have $\lambda > 0$, shrinking wedges have $\lambda < 0$, and static wedges have $\lambda = 0$. Table 1 summarized the values of the other dimensionless physical quantities.

τ_w represents shear stress along the stretched surface, q_w is the temperature flow, and q_m depicts mass flux in equation (2.12).

$$\begin{aligned}\tau_w = \mu_0 u_y \left[\beta^* + (1-\beta^*)(1 - \Gamma u_y)^{-1}\right]_{y=0}, \ q_w = -\left[\left(k + \frac{16\sigma T^3}{3k^*}\right)T_y\right]_{y=0}, \\ q_m = -D_B\left(C_y\right)_{y=0}.\end{aligned} \tag{2.12}$$

TABLE 1. Various Physical Parameters Values

S.No	Name of the Physical Parameters	Values of the Physical Parameters
1	Ratio of the viscosity	$\beta^* = \frac{\mu_0}{\mu_\infty}$
2	The effective thermal diffusivity	$\alpha = \frac{k}{\rho C_P}$
3	Weissenberg number	$We = \sqrt{\frac{\Gamma^2(m+1)u_e^3}{2\nu x}}$
4	Prandtl number	$Pr = \frac{\mu C_P}{k}$
5	Radiation parameter	$Rd = \frac{4\sigma^* T_\infty^3}{kk_1^*}$
6	Unsteadiness parameter	$A = \frac{c}{ax^{m-1}}$
7	The wedge angle parameter	$\beta = \frac{2m}{m+1}$
8	Hartmann number	$Ha^2 = \frac{\rho B_0^2}{ax^{m-1}}$
9	Lewis number	$Le = \frac{\nu}{D_B}$
10	Thermophoresis diffusion parameter	$Nt = \frac{\tau D_T(T_w - T_\infty)}{T_\infty \nu}$
11	Brownian motion parameter	$Nb = \frac{\tau D_B(C_w - C_\infty)}{\nu}$
12	Reynolds number	$Re_x = \frac{x u_e}{\nu}$
13	Skin friction	$C_{f_x} = \frac{\tau_w}{\rho U_w^2}$
14	Nusselt Number	$N_{u_x} = \frac{x q_w}{k(T_w - T_\infty)}$
15	Sherwood Number	$S_{h_x} = \frac{x q_m}{D_B(C_w - C_\infty)}$

The dimensionless local skin friction, local Nusselt number, and local Sherwood number are obtained with the help of Eq. (2.7) and Eq. (2.12).

$$
\begin{aligned}
C_{f_x}\sqrt{Re_x} &= \frac{1}{\sqrt{(2-\beta)}} f''(0)\left[\beta^* + (1-\beta^*)\left(1 - Wef''(0)\right)^{-1}\right], \\
\frac{N_{u_x}}{\sqrt{Re_x}} &= -\left(1 + \frac{4}{3}Rd\right)\theta'(0), \ and \ \frac{S_{h_x}}{\sqrt{Re_x}} = -\phi'(0).
\end{aligned}
\tag{2.13}
$$

3. Solution Methodology

For this evaluation, two different problem-solving techniques were covered and practiced. A numerical approach comes first, followed by a machine learning technique. The MATLAB package BVP4C solver to carry out the numerical solution technique. Higher-order achievable non-dimensional versions of ordinary differential equations are the source of first-order ODEs. It is the primary benefit of the MATLAB software BVP4C solver. The machine learning technique employed in the multiple linear regression method was the second phase of this research. Machine learning algorithms improve models by automatically producing forecasts or decision-making processes. Single prediction and multiple response variables showed a strong association, which led to the development of MLR, and the coefficient in which the different flow conditions affected each of them were all computed. In the end, the linear regression executed to determine the actual and anticipated values of skin friction (C_{f_x}), the Sherwood number (S_{h_x}), and the Nusselt number (N_{u_x}).

3.1. Numerical Approach.

The nonlinear ODEs are solved by the numerical procedure executed in the MATLAB programming language built with BVP4C computation. These ODEs represented by the equations ((2.8) - (2.10)) and Eq. (2.11) provided a set of boundary restrictions.

Gladwell et al. [34] created a MATLAB program to solve ordinary differential equations. The BVP4C solver implementing MATLAB software to solve boundary value problems for ordinary differential equations explored by L F Shampine et al. [35]. Computational modeling of Williamson fluid cross-flow over a porous shrinking/stretching surface involving a combination of hybrid nanofluid and thermal radiation based on the finite difference approach, as per a novel technique of this software identified by Umair Khan et al. [36]. This package for solving nonlinear ordinary differential equations along the curved moving surface produced by the time-dependent micro-rotational blood flow by conducting gold particles combined with the separate heat sources meticulously investigated by Y M Chu et al. [37]. The main advantage of this software was higher-order achievable nondimensional versions of the original equations converted into first-order ODEs.

For introducing the new variables are

$$f = y_1, f^{'} = y_2, f^{''} = y_3, \theta = y_4, \theta^{'} = y_5, \phi = y_6, \phi^{'} = y_7. \tag{3.1}$$

The variables listed above have changed in a dimensionless form of higher-order ODEs. These ODEs transformed into first-order ODEs.

$$y_1^{'} = y_2, \tag{3.2}$$

$$y_2^{'} = y_3, \tag{3.3}$$

$$y_3^{'} = \frac{-y_1 y_3 - \beta\left(1 - y_2^2\right) + A(2-\beta)\left(\frac{\eta}{2} y_3 + y_2 - 1\right) + Ha^2(2-\beta)(y_2 - 1)}{\left[\beta^* + \left(1 - \beta^*\right)\left(1 - We y_3\right)^{-2}\right]}, \tag{3.4}$$

$$y_4^{'} = y_5, \tag{3.5}$$

$$y_5^{'} = \frac{-y_1 y_5 + 2 y_2 y_4 + (\frac{A}{2})(2-\beta)\left(\eta y_5 + 3 y_4\right) - Nb y_5 y_7 - Nt y_5^2}{\left(\frac{1}{Pr}\right)\left(1 + \frac{4}{3} Rd\right)}, \tag{3.6}$$

$$y_6^{'} = y_7, \tag{3.7}$$

$$y_7^{'} = \frac{-(\frac{1}{Le})(\frac{Nt}{Nb}) y_5^{'} + (\frac{A}{2})(2-\beta)(\eta y_7 + 3 y_6) + 2 y_2 y_6 - y_1 y_7}{(\frac{1}{Le})}, \tag{3.8}$$

Moreover, the boundary constraints are

$$\begin{aligned} y_{a_1} = 0, y_{a_2} = \lambda, y_{a_4} = 1, y_{a_6} = 1, \\ y_{b_2} = 1, y_{b_4} = 0, y_{b_6} = 0. \end{aligned} \tag{3.9}$$

The system of Eqs. ((3.2) - (3.8)) and the accompanying boundary condition Eq. (3.9) is solved by computationally adopting the BVP4C. The first-order ODE system adapted the upper-third-order and second-order achievable nondimensional forms of ODEs to employ the BVP4C approach. The preceding technique needed an initial estimation at the mesh point. This approach offered the advantage of the outcomes in higher-order form. Several physical parameters were affected by velocity, temperature, and concentration, as well as skin friction, Nusselt number, and Sherwood number values are determined and displayed in the form of tables and graphs.

3.2. **Machine Learning Approach.**

3.2.1. *Data Description.* Machine learning is a branch of artificial intelligence that evaluates data to support computers in learning new concepts and tasks more effectively. It affected training data in a model by automating forecasting or decision-making procedures. To extract useful information from a vast volume of data for further applications or a deeper comprehension of the underlying flow mechanism, machine Learning offers a multitude of analytical techniques. Firuz Kamalov et al.([38] -[39]) explored the applications of machine learning. In addition, machine learning algorithms can automatically be active flow management and optimization, which can also improve the flow of information. Palash Sharma et al. [40] developed for artificial learning mathematical computing models. A hybrid nanofluid flow on a significantly expanding surface with heat source-sink effects employing regression suggested by C Sulochana et al. [41]. Many different methods exist for regression and classification. After examining the prevalence of ML models in that area, the multiple linear regression technique was used in this work to anticipate the physical properties of fluid flow ([42] - [45]). In this regard, the current paper examined three distinct data points obtained from the numerical results for 19 observations from skin friction, 13 data from the Nusselt number, and 11 from the Sherwood number.

3.2.2. *Multiple Linear Regression Algorithm.* The significant association between one prediction variable and several response variables ultimately resulted in the development of MLR. The data analysis multiple regression model has two primary benefits. The first skill is determining the relative influence of one or more predictor variables on the criterion value. The capacity to spot errors or deviations is the second benefit. In this investigation, multiple linear regression occurs to predict the skin friction coefficient, Nusselt number, and Sherwood number by employing several physical parameters.
Prediction formula for skin friction coefficient,
$C_{f_x} = 1.2428 + 0.026057 * \beta + 0.4807 * \lambda - 0.78901 * We + 0.28027 * \beta^* + 0.26714 * Ha + 0.029986 * A$
Prediction formula for Nusselt number,
$N_{u_x} = 4.2692 - 0.24647 * \beta - 0.062507 * Pr - 0.79125 * Nb - 0.92853 * Nt - 0.43981 * Rd - 0.050073 * A$
Prediction formula for Sherwood number,
$S_{h_x} = 0.44806 - 0.51344 * \beta + 0.37639 * Nb - 0.88295 * Nt + 0.68183 * Le + 0.25916 * A$

3.2.3. *Simple Linear Regression Algorithm.* A goal of the simple linear regression model is the best-fitting straight line through the data points that minimizes the sum of squared error, which is a statistical method that allows us to summarize and study if there is a linear relationship between the independent (x) and dependent (y) variables. A single independent variable was employed in this evaluation to predict a single dependent variable. The simple linear regression line equation is
$y = \beta_0 + \beta_1 x + e.$

Here, the independent variable is x, and the dependent variable is y, the intercept of the regression line on the vertical axis constant term β_0, and the slope of the regression line regression coefficient β_1, and the random error e.

In this section, we incorporated skin friction, Nusselt number, and Sherwood number actual results together with predicted outcomes from multiple linear regression to confirm the accuracy of the estimation process.

4. Results and Discussion

The current section explored the effects of various parameter settings on the outcomes. Misra et al. [46], Valvano et al. [47], and Chato et al. [48] acquired the subsequent data $T = 310K, \mu = 3.2 * 10^{-3}(Kg/m.s), Cp = 14.65(J/Kg.K), k = 2.2*10^{-3}(J/m.s.K)$ are the temperature values. The value of the Prandtl number $Pr = \frac{\mu Cp}{k}$ for human blood is 21. The set of nonlinear ODEs with boundary conditions Eqs. ((2.8) - (2.11)) by implementing the BVP4C solver in the MATLAB package. The associated parameters with the following values are listed as follows: $\beta = 0.2, We = 0.5, Ha = 0.5, A = 1.0, Pr = 21, Nt = 0.5, Nb = 0.5, Rd = 0.5, Le = 0.5, \lambda = 0.1$.

The comparative statistics for different values of the β on skin friction coefficient by Kuo et al. [26], Ishaq et al. [27], Aamir Hamid et al. [28], and K Subbarayudu et al. [29] were presented in Table 2. The initial phase of the exploration focused on the velocity distribution, the temperature description, and the concentration distribution, as well as changes in the skin friction, Nusselt number, and the Sherwood number impacts of several physical parameters. Furthermore, to establish that the novelty of this research is the machine learning component of a multiple linear regression model for the physical quantities of skin friction, Nusselt number, and Sherwood number, as well as to validate the numerical data and expected values for implementing the linear regression model.

Table 2. Comparative statistics for various β values on Skin friction coefficient $\sqrt{Re_x}C_{f_x}$

β	Kuo [26]	Ishaq [27]	Aamir Hamid [28]	Subbarayudu K. [29]	Present Result
0.0	0.469600	0.4696	0.469600	0.4696	0.4696
0.1	0.587080	0.5870	0.587035	0.5869	0.5870
0.3	0.774724	0.7748	0.774755	0.7747	0.7748
0.5	0.927905	0.9277	0.927680	0.8543	0.9277
0.9	1.232589	1.2326	1.232588	0.9392	1.1777

4.1. **Impact of Velocity profile.**

The essential concepts of velocity distribution affected the description of fluid flow for the several physical features depicted in Figures (3 to 7). The viscosity ratio parameter affects the boundary layer, the region near the wall where the fluid velocity changes rapidly, which represents the boundary layer in the upper zone being thicker than the lower region, $\beta^*(0.0, 0.2, 0.4, 0.6)$ raised, and the intensity of blood circulation developed as shown in Figure 3.

The increment of Hartmann number $Ha(0.5, 1.0, 1.5, 2.0)$ enhanced the blood flow frequency displayed in Figure 4 due to improved magnetic field and reduced the flow resistance.

Figure 5 suggested that a positive Weissenberg number $We(0.5, 1.0, 1.5, 2.0)$ resulted in a less extensive momentum dispersion of blood circulation. From the scientific perspective, a more substantial Weissenberg number means the fluid will take longer to return to its original state after being distorted.

The velocity distribution increased for the advancement of the wedge angle parameter $\beta(0.1, 0.2, 0.3, 0.4)$ offered in Figure 6. If caused by the growing distance from the wedge tip, the outside velocity accelerates quickly as the wedge angle parameter expands, and the fluid close to the wedge surface must accelerate more, leading to a faster travel speed indicated by increases in blood flow.

The velocity profile strengthened for the improvement of unsteadiness parameter $A(1.0, 1.1, 1.2, 1.3)$ demonstrated in Figure 7. Physically, it increases the slip velocity at the wall, optimizes the fluid acceleration and the diffusion of nanoparticles, and there was an expansion in blood circulation rate.

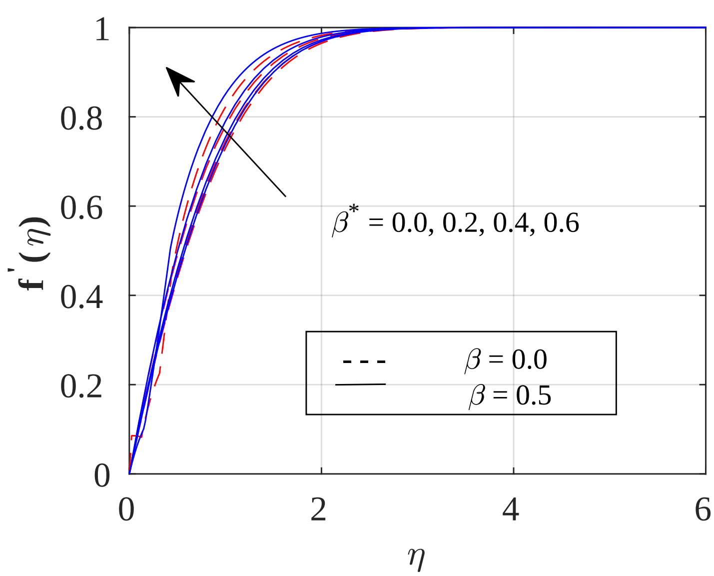

FIGURE 3. Impact of β^* on $f'(\eta)$ values

4.2. **Impact of temperature profile.** The impact of temperature variations on fluid behavior and the possibilities for temperature adjustment method are extensively explored in Figures (8 - 13). Figure 8 depicted the temperature distribution extended the greater values of wedge angle parameters $\beta(0.1, 0.2, 0.3, 0.4)$. From a physical standpoint, a larger wedge angle means higher thermal conductivity, then upgraded the thickness of the thermal boundary layer and the heat flux at the surface, for the blood fluid temperature generates more heat.

The rapid temperature blood flow away from the wedge, representing the scientific point of view, the particles in a fluid migrate quicker towards hot or

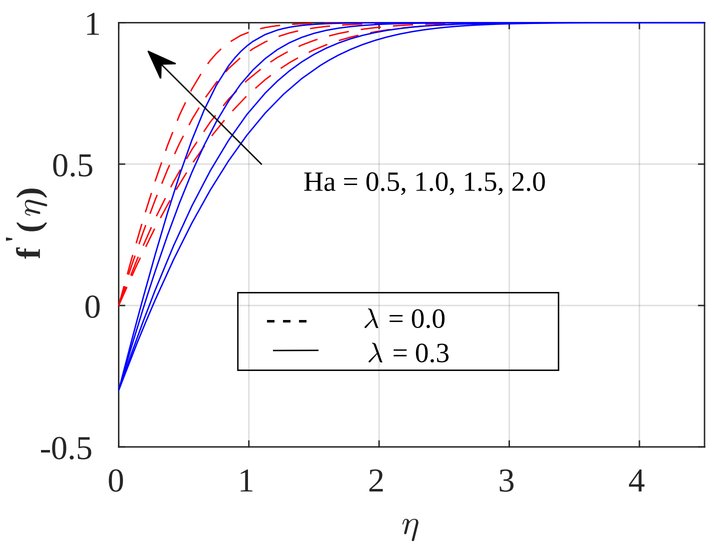

FIGURE 4. Impact of Ha on $f'(\eta)$ values

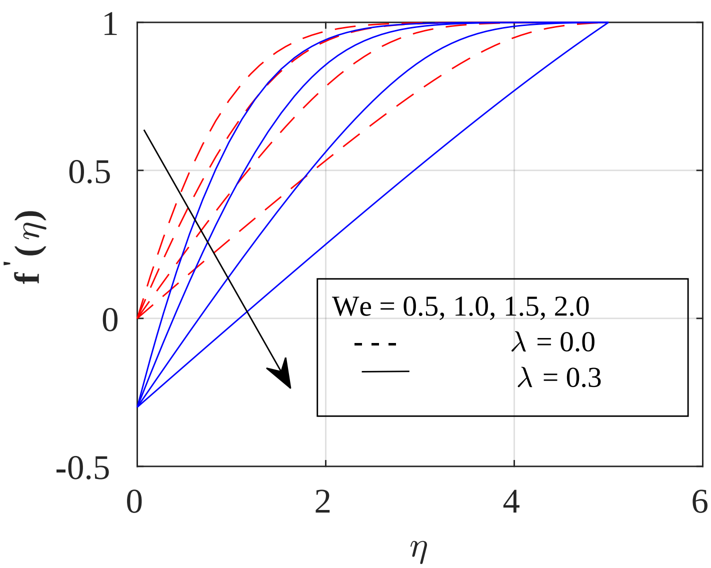

FIGURE 5. Impact of We on $f'(\eta)$ values

cold regions for a maximum temperature gradient. Therefore, the improvement of thermophoresis diffusion $Nt(0.0, 0.1, 0.2, 0.3)$ boosted the temperature profile demonstrated in Figure 9.

The larger values of the Brownian motion $Nb(0.3, 0.5, 0.7, 0.9)$ denoted the more heat transportation captured in Figure 10. Scientifically, plasma molecules travel quickly and collide with particles regularly. It occurs, resulting in several effects

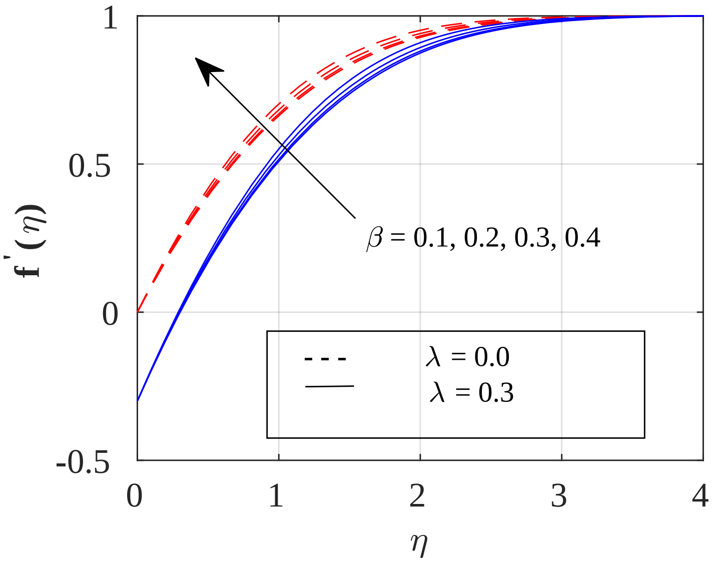

FIGURE 6. Impact of β on $f'(\eta)$ values

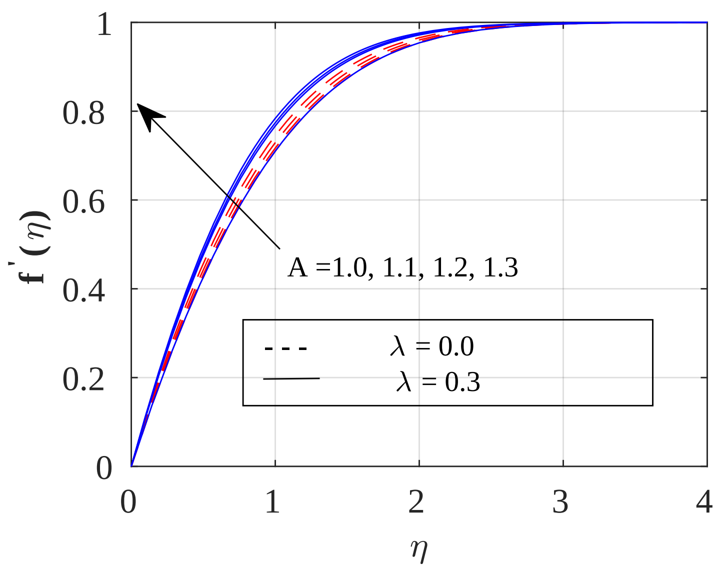

FIGURE 7. Impact of A on $f'(\eta)$ values

on blood flow, including increased blood pressure, heart rate, and oxygen delivery to tissues.

Figure 11 displayed that the temperature profile improved as the positive thermal radiation parameter $Rd(0.5, 1.0, 1.5, 2.0)$. Because of the maximum temperature of the blood fluid, the fluid near the surface has more heat by minimizing heat loss from the blood to the blood vessel wall or the surrounding fluid.

The enhancement of the Prandtl number leads to the greater temperature gradient caused by the minimum temperature of blood circulation. Physically, with a lower thermal diffusivity, the heat moves through the fluid more slowly and does not absorb heat from the surroundings as quickly. It indicates the development of $Pr(1.0, 3.0, 5.0, 7.0)$ reduces the temperature profile presented in Figure 12.

In terms of science, the increment of unsteadiness parameter $A(1.0, 1.1, 1.2, 1.3)$, the magnetic field parameter is heavier, thus, repeatedly disturbs fluid flow illustrated in Figure 13. It represents that a fluid close to the surface is affected by the more potent temperature gradient, resulting in the average temperature of blood circulation dropping.

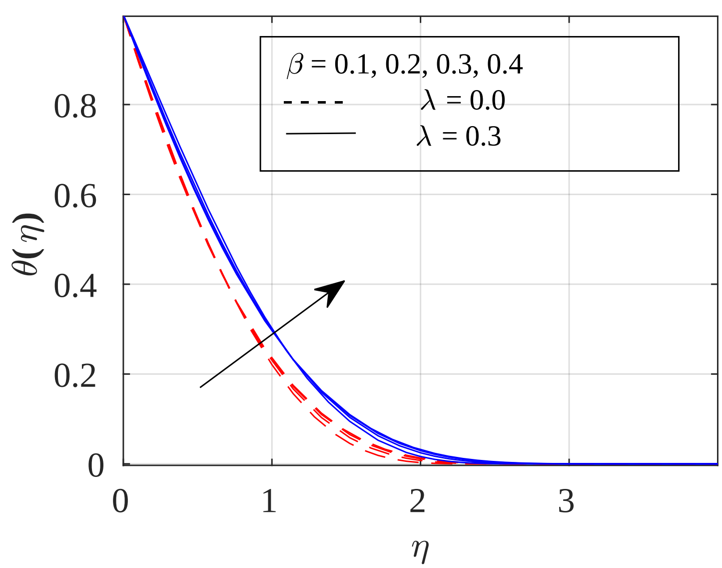

FIGURE 8. Impact of β on $\theta(\eta)$ values

4.3. **Impact of Concentration profile.** Figures (14-18) demonstrated that the concentration profile entirely impacts the rate at which the fluid flows on the mass transfer. Figure 14 provided the development of wedge angle parameters $\beta(0.1, 0.2, 0.3, 0.4)$ indicated that the blood flow disperses blood particles such as red blood cells, white blood cells, platelets, and plasma proteins more. It improved the concentration of blood along the wall and the gradients of blood particles along the flow direction.

The enhancement of thermophoresis diffusion $Nt(0.0, 0.1, 0.2, 0.3)$ caused an improvement in the efficiency of the blood flow because the fluid particles move away from the hot zone and accumulate in the cold region identified in Figure 15.

The Brownian motion parameters $Nb(0.3, 0.5, 0.7, 0.9)$ strengthened when the decrement of concentration distribution was mentioned in Figure 16. Due to the concentration gradient and heat transfer rate decreased, the nano-particles in the blood dispersed and became less crowded, representing a lower level of blood circulation.

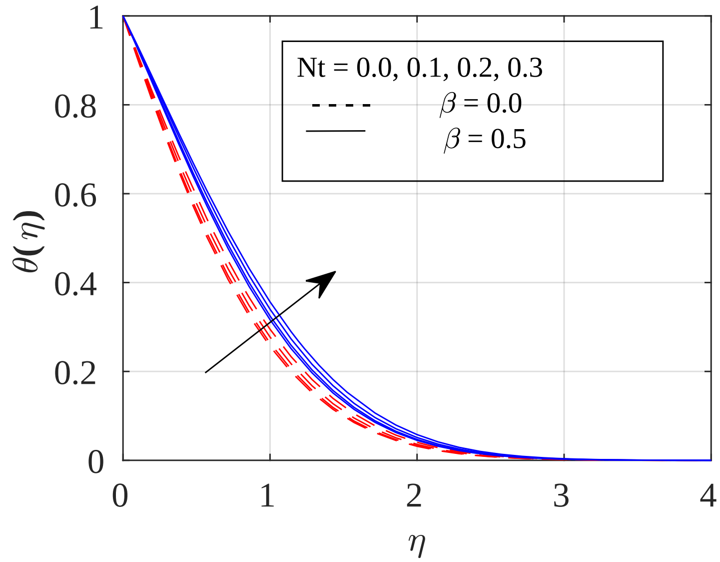

FIGURE 9. Impact of Nt on $\theta(\eta)$ values

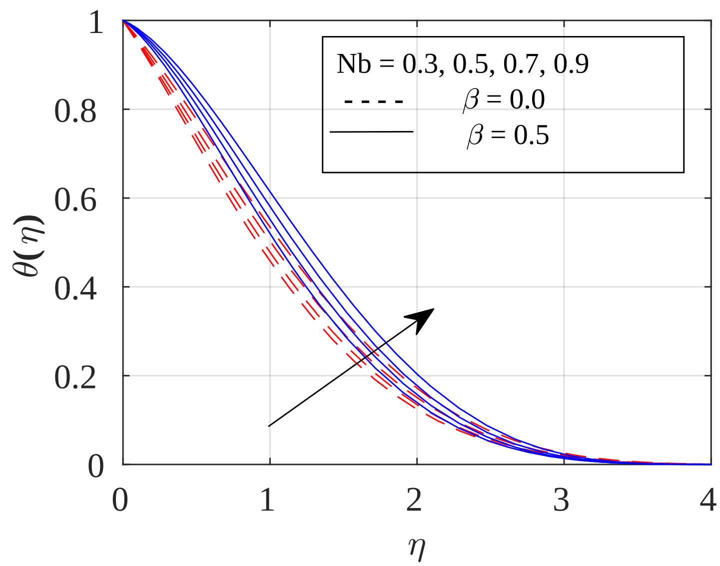

FIGURE 10. Impact of Nb on $\theta(\eta)$ values

The temperature gradient is superior to the concentration gradient, thermal diffusivity exceeds the mass diffusivity, and the thermal boundary layer is thin for the Lewis number $Le(0.5, 1.0, 1.5, 2.0)$ becomes higher. As a result, the quantity of blood flow dropped, as shown in Figure 17.

Figure 18 portrayed that the concentration boundary layer thickness reduced as the unsteadiness parameter $A(1.0, 1.1, 1.2, 1.3)$ elevated. Physically, the flow is more unstable, and the particles diffuse faster from the surface to the free stream,

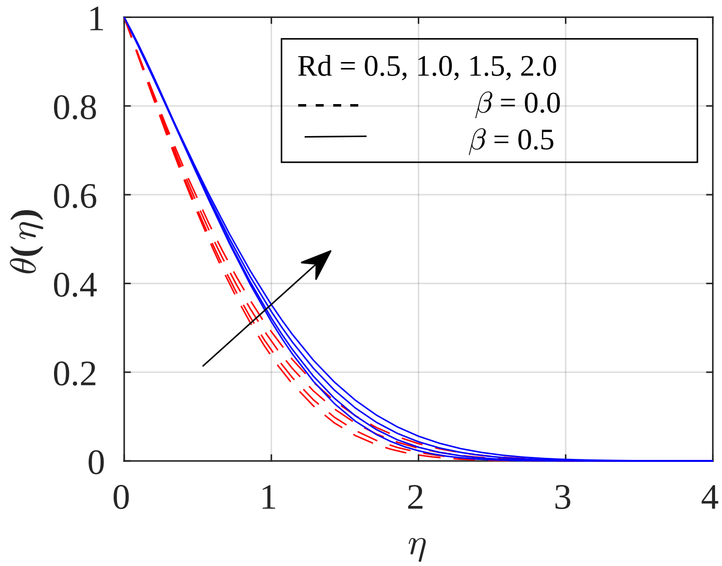

FIGURE 11. Impact of Rd on $\theta(\eta)$ values

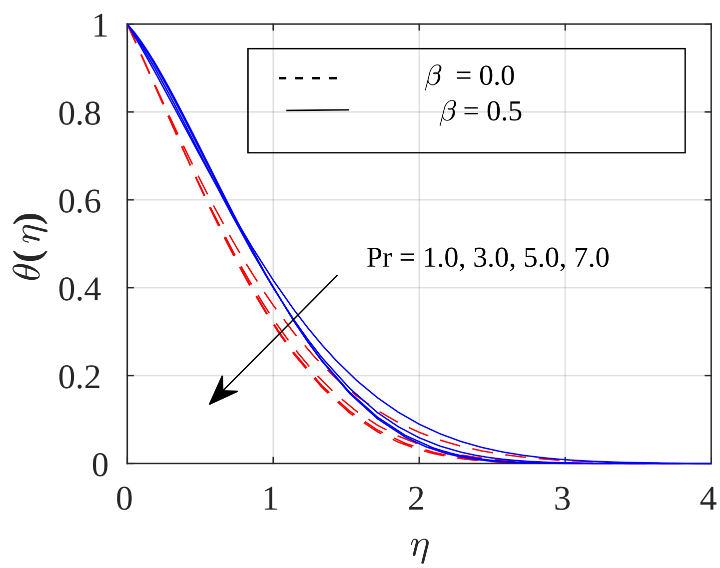

FIGURE 12. Impact of Pr on $\theta(\eta)$ values

resulting in a lower concentration gradient and a thinner concentration boundary layer. The mass transfer rate at the surface also weakened as the concentration of blood particles in the fluid declined.

4.4. **Impact of skin friction coefficient.** Table 3 illustrated that the skin friction coefficient affected the several physical parameter values of β, λ, We, β^*, Ha, and A. The wedge angle parameter $\beta(0.2, 0.3, 0.4, 0.5)$ boosted for the skin friction improved. A wide wedge reflects more flow and increases the pressure gradient

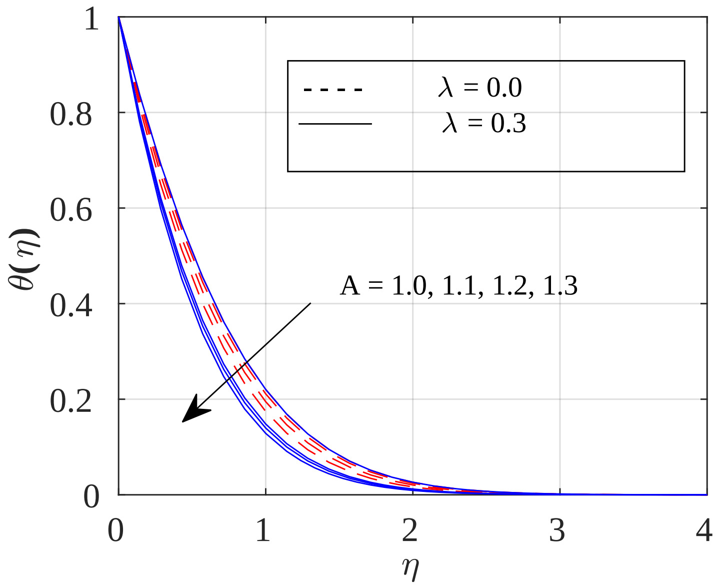

FIGURE 13. Impact of A on $\theta(\eta)$ values

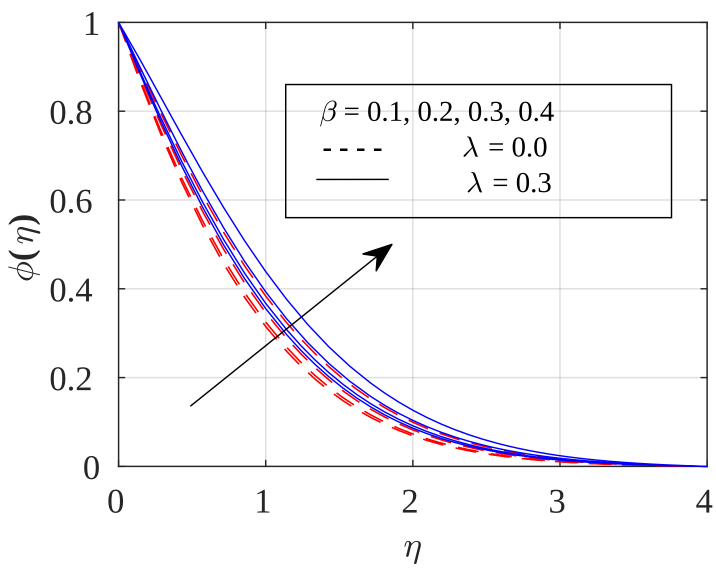

FIGURE 14. Impact of β on $\phi(\eta)$ values

along the surface. Because the velocity gradient near the wall accelerates, and there is a small amount of blood circulation.

The development of skin friction, the wedge moving parameter $\lambda(0.1, 0.2, 0.3, 0.4)$ grew. A larger λ represents a stronger pressure gradient, which reduces the fluid towards the surface. As a result, it reduced blood flow, demonstrating that blood viscosity declined as the shear rate upgraded.

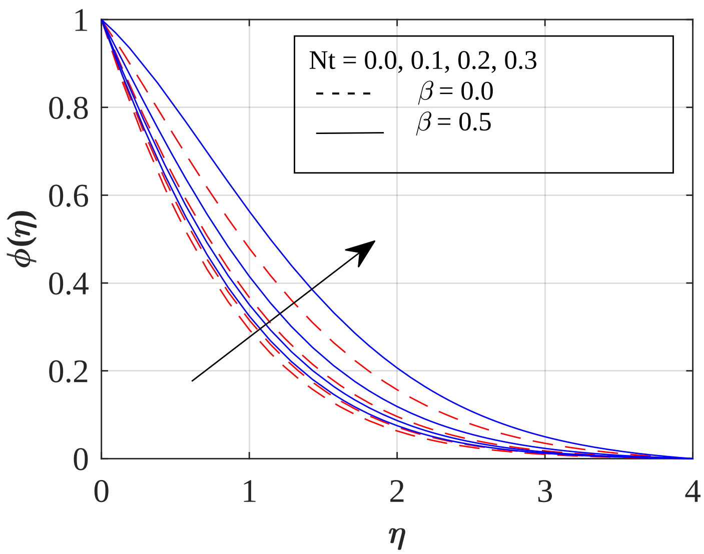

FIGURE 15. Impact of Nt on $\phi(\eta)$ values

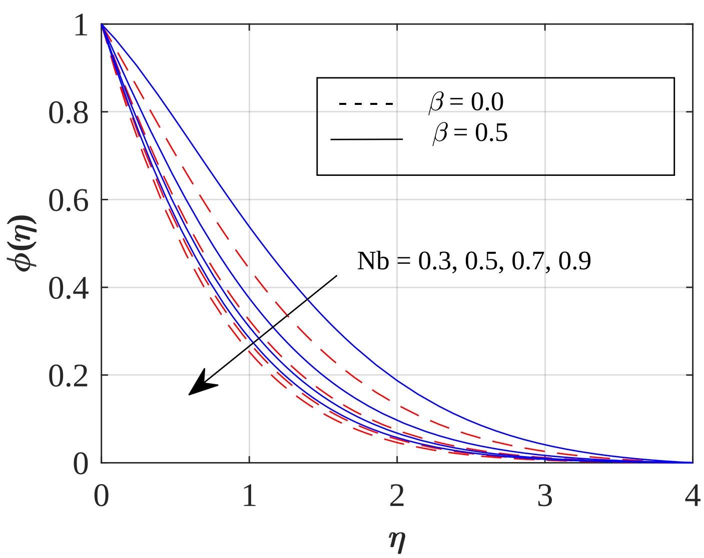

FIGURE 16. Impact of Nb on $\phi(\eta)$ values

The skin friction dropped for the higher Weissenberg number $We(0.5, 0.6, 0.7, 0.8)$. This reduction for several non-Newtonian fluid types (the tangent hyperbolic fluid and the Williamson fluid, in particular) increases with the Weissenberg number for more elastic and capable of stretching or deforming quickly. According to the physical standpoint, a fluid with a higher Weissenberg number should deform more rapidly and have a thinner boundary layer close to the skin due to less shear stress for improved blood circulation.

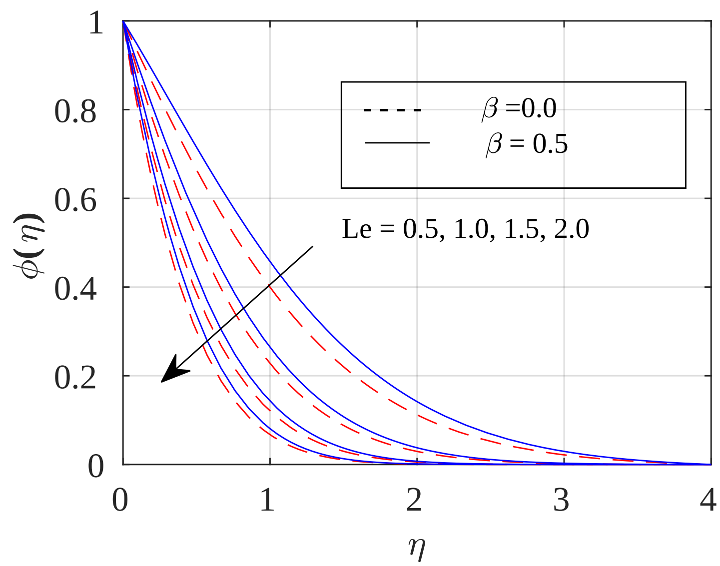

FIGURE 17. Impact of Le on $\phi(\eta)$ values

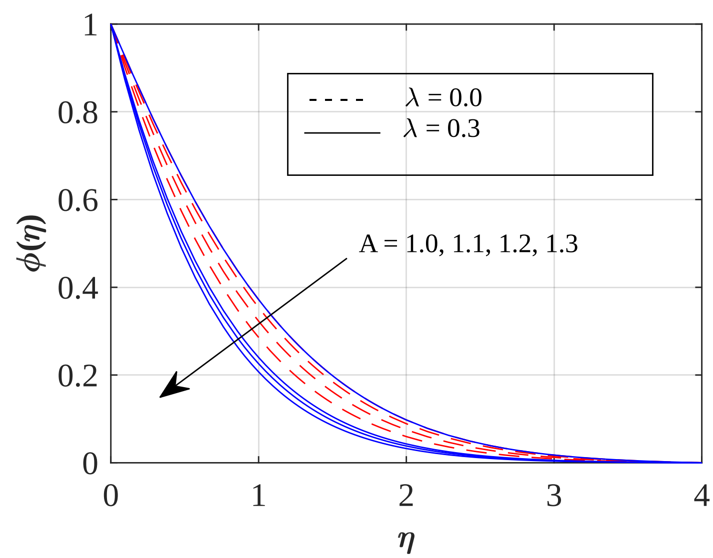

FIGURE 18. Impact of A on $\phi(\eta)$ values

The viscosity ratio $\beta^*(0.2, 0.3, 0.4, 0.5)$ raises for improved skin friction because chains of several red blood cells become more resistant to shear stress and more aligned with the flow direction. Therefore, the lower amount of blood flow.

Skin friction coefficient values increased for larger values of Hartmann number $Ha(0.5, 1.0, 1.5, 2.0)$ means the frequency of blood circulation decreased from the scientific point, for a stronger magnetic field resists fluid motion and increases surface drag force.

The blood is an electrically conducting fluid to increased magnetic force for the unsteadiness parameter $A(1.0, 1.1, 1.2, 1.3)$ improves. This force resists fluid motion, increasing skin friction and slowing the intensity of the blood flow.

TABLE 3. Various parameters of $\beta, \lambda, We, \beta^*, Ha, A$ on skin friction coefficient C_{f_x}

β	λ	We	β^*	Ha	A	$f''(0)$
0.2	0.1	0.5	0.2	0.5	1.0	1.1261
0.3	0.1	0.5	0.2	0.5	1.0	1.1264
0.4	0.1	0.5	0.2	0.5	1.0	1.1267
0.5	0.1	0.5	0.2	0.5	1.0	1.1280
0.2	0.1	0.5	0.2	0.5	1.0	1.1261
0.2	0.2	0.5	0.2	0.5	1.0	1.1754
0.2	0.3	0.5	0.2	0.5	1.0	1.2202
0.2	0.4	0.5	0.2	0.5	1.0	1.2615
0.2	0.1	0.5	0.2	0.5	1.0	1.1261
0.2	0.1	0.6	0.2	0.5	1.0	1.0367
0.2	0.1	0.7	0.2	0.5	1.0	0.9583
0.2	0.1	0.8	0.2	0.5	1.0	0.8898
0.2	0.1	0.5	0.2	0.5	1.0	1.1261
0.2	0.1	0.5	0.3	0.5	1.0	1.1520
0.2	0.1	0.5	0.4	0.5	1.0	1.1816
0.2	0.1	0.5	0.5	0.5	1.0	1.2015
0.2	0.1	0.5	0.2	0.5	1.0	1.1261
0.2	0.1	0.5	0.2	1.0	1.0	1.2587
0.2	0.1	0.5	0.2	1.5	1.0	1.3974
0.2	0.1	0.5	0.2	2.0	1.0	1.5146
0.2	0.1	0.5	0.2	0.5	1.0	1.1261
0.2	0.1	0.5	0.2	0.5	1.1	1.1041
0.2	0.1	0.5	0.2	0.5	1.2	1.1220
0.2	0.1	0.5	0.2	0.5	1.3	1.1404

4.5. **Impact of Nusselt Number.** The Nusselt number is a dimensionless quantity that compares convective to conductive heat transfer over a boundary layer, for this impact involves a wide range of physical characteristics such as β, Pr, Nb, Nt, Rd, and A demonstrated in Table 4. A lower Nusselt number and a higher wedge angular parameter $\beta(0.2, 0.3, 0.4)$ depicted that increased the heat loss and the drag force of the wedge, the reduction of convective heat transfer from the fluid to the wedge surface represents the highest temperature of the blood flow.

The enhancement of Prandtl number $Pr(21, 22, 23)$ suggests that the thermal boundary layer is more restricted than the velocity boundary layer, leading to decreases in the Nusselt number, more heart temperature of the blood flow because greater heat transfer rate and a larger recirculating enhanced the fluid velocity and dropped the viscous drag.

The blood flow temperature developed for the Nusselt number values minimized when the improvement of Brownian Motion $Nb(0.5, 1.0, 1.5)$. Physically, the zigzag motion of particles in the fluid reduces the effective thermal conductivity and increases the thermal boundary layer thickness.

The Nusselt number declined as the thermophoresis diffusion parameter Nt(0.5, 1.0, 1.5) elevated this phenomenon due to the thermophoretic force causing the nano-particles to move away from the hot region and accumulate near the cold region, and improves the blood fluid temperature.

The radiation parameter and the Nusselt number have a negative correlation. The value of $Rd(0.5, 1.0, 1.5)$ increased when the Nusselt number reduced scientifically the thermal radiation enhancing the temperature and the thermal boundary layer thickness of the fluid. Maximum radiation parameters caused a more extensive thermal radiation effect and a much greater heat transfer rate for the maximum temperature of blood circulation.

The enhancement of unsteadiness parameter $A(1.0, 1.1, 1.2)$ depicted the Nusselt number improved because the unsteady flow increases the heat transfer coefficient and the temperature gradient at the wall. It demonstrated that the convective heat transfer rate is greater when the improvement of the unsteadiness parameter leads to a lower blood fluid temperature.

Table 4. Various parameters of β, Pr, Nb, Nt, Rd, A on Nusselt Number N_{u_x}

β	Pr	Nb	Nt	Rd	A	$-\theta'(0)$
0.2	21	0.5	0.5	0.5	1.0	1.8220
0.3	21	0.5	0.5	0.5	1.0	1.7712
0.4	21	0.5	0.5	0.5	1.0	1.7188
0.2	21	0.5	0.5	0.5	1.0	1.8220
0.2	22	0.5	0.5	0.5	1.0	1.7101
0.2	23	0.5	0.5	0.5	1.0	1.6547
0.2	21	0.5	0.5	0.5	1.0	1.8220
0.2	21	1.0	0.5	0.5	1.0	1.2883
0.2	21	1.5	0.5	0.5	1.0	1.0328
0.2	21	0.5	0.5	0.5	1.0	1.8220
0.2	21	0.5	1.0	0.5	1.0	1.4073
0.2	21	0.5	1.5	0.5	1.0	0.8017
0.2	21	0.5	0.5	0.5	1.0	1.8220
0.2	21	0.5	0.5	1.0	1.0	1.5015
0.2	21	0.5	0.5	1.5	1.0	1.3655
0.2	21	0.5	0.5	0.5	1.0	1.8220
0.2	21	0.5	0.5	0.5	1.1	1.7244
0.2	21	0.5	0.5	0.5	1.2	1.7913

4.6. **Impact of Sherwood Number.** Variations in Sherwood number have several impacts on various physical parameters of β, Nb, Nt, Le, and A at different levels, as displayed in Table 5. It is a dimensionless quantity that compares convective mass transfer to mass diffusivity. The minimum Sherwood number for larger values of Wedge angular parameter $\beta(0.2, 0.3, 0.4)$. It means that the wedge angle increased the fluid velocity and the momentum boundary layer thickness, which reduced the concentration gradient, and the mass transfer coefficient at the wall indicated a higher intensity of blood circulation.

The convective mass transfer rate was raised when the blood flow concentration gradient dropped to increase the mass transfer coefficient at the wall. Thus, the Sherwood number developed when greater values of the Brownian motion parameter $Nb(0.5, 1.0, 1.5)$.

Sherwood number decreased for the development of thermophoresis diffusion $Nt(0.5, 0.7, 1.1)$ because the thermophoretic force causes the nano-particles to migrate away from the hot wall and accumulate near the cold wall. A negative link between the Sherwood number and thermophoresis diffusion leads to a reduced concentration gradient, in which the convective mass transfer rate is more downward for the superior concentration of blood circulation.

The Lewis number $Le(0.5, 1.0, 1.5)$ climbed as the Sherwood number value expanded. Practically, the stronger Lewis number indicated that the fluid had a greater thermal diffusivity than mass diffusivity, which means that the temperature gradient was more than the concentration gradient due to the lower quantity of blood flow.

Sherwood number elevated for the unsteadiness parameter $A(1.0, 1.1, 1.2)$ raised because of the thickness of the concentration boundary layer, the area where the variation of the fluid concentration quickly. The concentration gradient near the surface increases, implying a thinner concentration boundary layer due to the intensity of the blood circulation minimized.

TABLE 5. Various parameters of β, Nb, Nt, Le, A on Sherwood Number S_{h_x}

β	Nb	Nt	Le	A	$-\phi'(0)$
0.2	0.5	0.5	0.5	1.0	0.6532
0.3	0.5	0.5	0.5	1.0	0.6264
0.4	0.5	0.5	0.5	1.0	0.5967
0.2	0.5	0.5	0.5	1.0	0.6532
0.2	1.0	0.5	0.5	1.0	0.9457
0.2	1.5	0.5	0.5	1.0	1.0359
0.2	0.5	0.5	0.5	1.0	0.6532
0.2	0.5	0.7	0.5	1.0	0.5018
0.2	0.5	1.1	0.5	1.0	0.1670
0.2	0.5	0.5	0.5	1.0	0.6532
0.2	0.5	0.5	1.0	1.0	1.0927
0.2	0.5	0.5	1.5	1.0	1.3442
0.2	0.5	0.5	0.5	1.0	0.6532
0.2	0.5	0.5	0.5	1.1	0.7039
0.2	0.5	0.5	0.5	1.2	0.7511

4.7. **Machine Learning with MLR.** Machine learning employed various linear regression techniques to obtain accurate anticipated values from existent data. The potential of a machine learning system predicted accuracy for physical parameters such as skin friction, Nusselt number, and Sherwood number. Additionally, Furthermore, this novel technique is essential in minimizing error tolerance. Multiple linear regression has an extensive effect on many biological domains. The current article had a significant impact on the biomedical area. In this aspect, it analyses the blood flow and correctly identifies cancer cells.

Figure 19 highlighted the outcomes of a research study into the impact of skin friction on the Hartmann and Weissenberg numbers. The Nusselt number effects of thermophoresis diffusion and Prandtl number are demonstrated in Figure 20. Figure 21 suggested the Sherwood number impact of the Lewis number and Brownian motion.

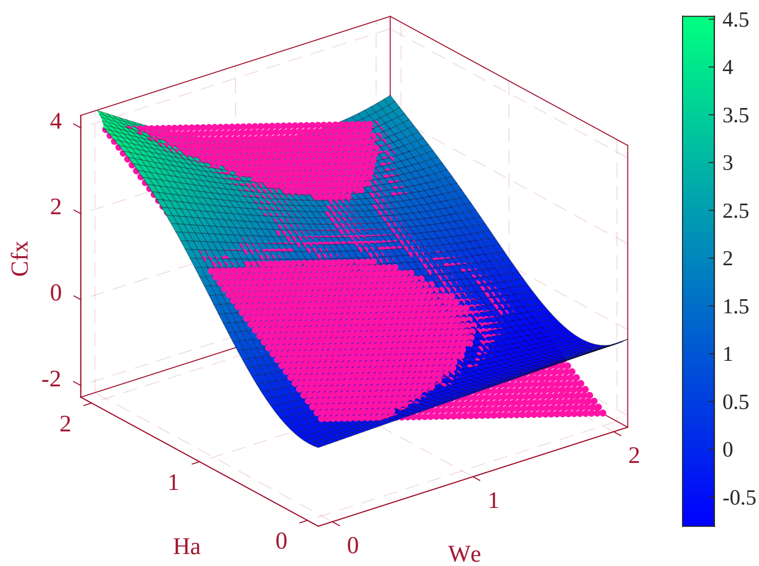

FIGURE 19. Skin friction coefficient effects with Hartmann number and Weissenberg number

To compare model results to anticipated data by making predictions based on unknown observations, an accurate approximation of fitted is executed. The accuracy of data prediction confirmed all machine learning algorithms, and the actual and predicted values are comparable. Figures (22 -24) displayed that skin friction, Nusselt number, and Sherwood number impact the numerical and predicted values of a simple linear regression model.

Tables (6 - 8) investigated the assessment results for the skin friction, Nusselt number, and Sherwood number effects of response and predicted values of multiple linear regression.

The standard errors of the physical quantities of skin friction, Nusselt number, and Sherwood number were 0.00199, 0.020025, and 0.014774, respectively. Table 9 expressed the tolerance for the accuracy level of fitted multiple linear regression. The values of standard error and root mean square error are small, and the values of R^2 and adjusted R^2 are approximately equal to 1, indicating the quality of fitted multiple linear regression.

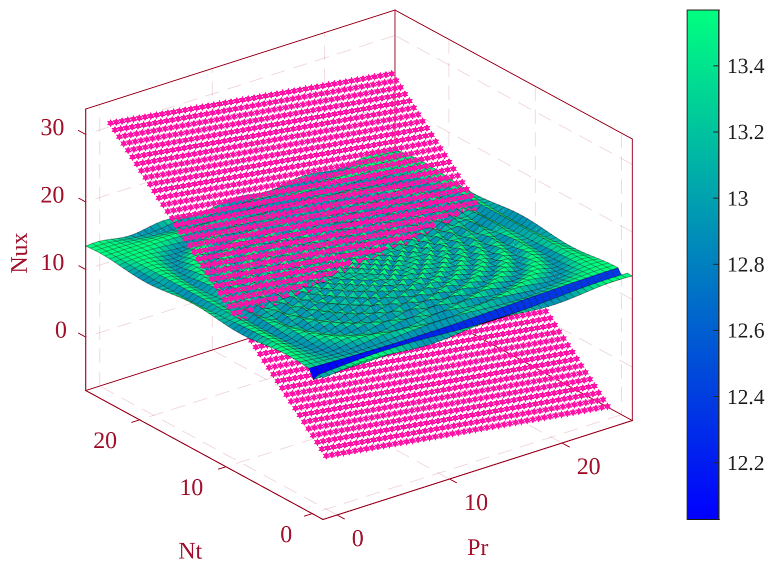

FIGURE 20. Nusselt number effects with Prandtl number and Thermophoresis diffusion

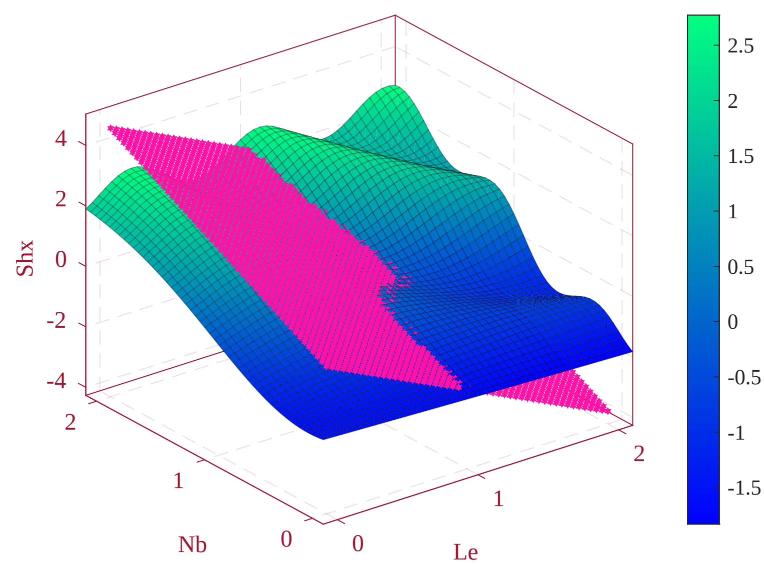

FIGURE 21. Sherwood number effects with Lewis number and Brownian motion

The linear regression evidence for existing and anticipated values of skin friction, Nusselt number, and Sherwood number demonstrated in Tables (10 - 12).

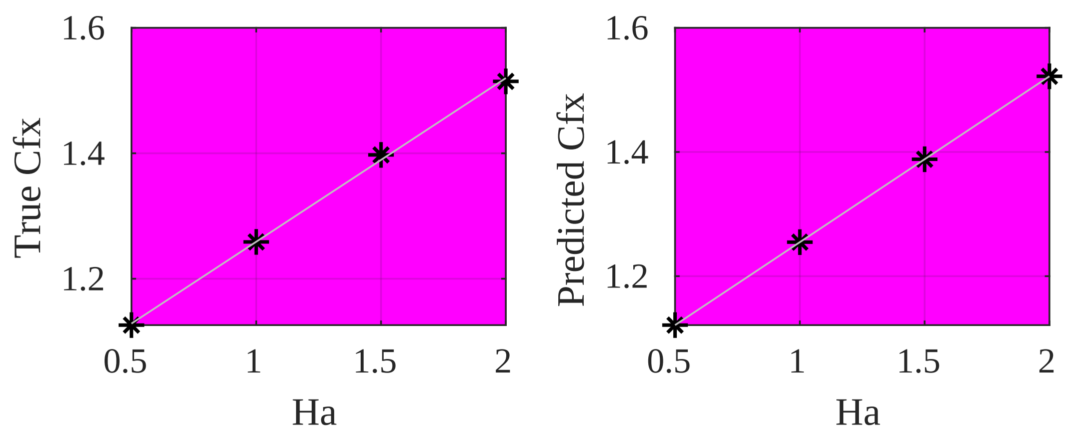

Figure 22. Skin friction impacts of true and predicted values

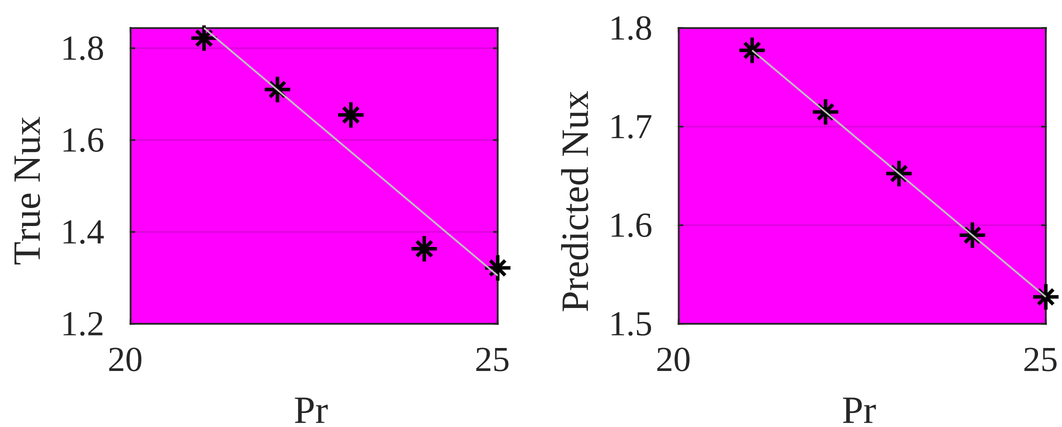

Figure 23. Nusselt number impacts of true and predicted values

5. Conclusion

- The present work explores the radiative effects of an unstable MHD Williamson blood fluid flow through a wedge affected by thermophoresis diffusion and Brownian motion. It accomplishes this by employing numerical and machine-learning techniques to analyze the velocity, temperature, and concentration distributions with various physical parameters. The following are some noteworthy observations:

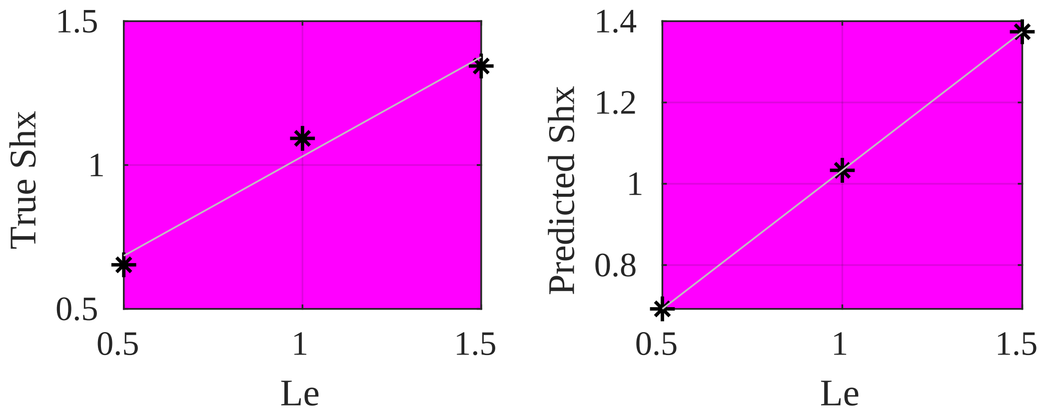

Figure 24. Sherwood number impacts of true and predicted values

Table 6. MLR Data for Skin friction coefficient

β	λ	We	β^*	Ha	A	True Values	Predicted Values
0.2	0.1	0.5	0.2	0.5	1.0	1.1261	1.1212
0.3	0.1	0.5	0.2	0.5	1.0	1.1264	1.1238
0.4	0.1	0.5	0.2	0.5	1.0	1.1267	1.1264
0.5	0.1	0.5	0.2	0.5	1.0	1.1280	1.1290
0.2	0.2	0.5	0.2	0.5	1.0	1.1754	1.1693
0.2	0.3	0.5	0.2	0.5	1.0	1.2202	1.2173
0.2	0.4	0.5	0.2	0.5	1.0	1.2615	1.2654
0.2	0.1	0.6	0.2	0.5	1.0	1.0367	1.0423
0.2	0.1	0.7	0.2	0.5	1.0	0.9583	0.9634
0.2	0.1	0.8	0.2	0.5	1.0	0.8898	0.8845
0.2	0.1	0.5	0.3	0.5	1.0	1.1520	1.1492
0.2	0.1	0.5	0.4	0.5	1.0	1.1816	1.1772
0.2	0.1	0.5	0.5	0.5	1.0	1.2015	1.2053
0.2	0.1	0.5	0.2	1.0	1.0	1.2587	1.2548
0.2	0.1	0.5	0.2	1.5	1.0	1.3974	1.3883
0.2	0.1	0.5	0.2	2.0	1.0	1.5146	1.5219
0.2	0.1	0.5	0.2	0.5	1.1	1.1041	1.1242
0.2	0.1	0.5	0.2	0.5	1.2	1.1220	1.1272
0.2	0.1	0.5	0.2	0.5	1.3	1.1404	1.1302

- Positive Hartmann number variation for improved the velocity of blood flow by minimizing viscous drag and increasing fluid acceleration.
- The development of the Weissenberg number dropped the frequency of blood circulation due to the fluid having greater flexibility and resistance.

Table 7. MLR Data for Nusselt number

β	Pr	Nb	Nt	Rd	A	True Values	Predicted Values
0.2	21	0.5	0.5	0.5	1.0	1.8220	1.7774
0.3	21	0.5	0.5	0.5	1.0	1.7712	1.7527
0.4	21	0.5	0.5	0.5	1.0	1.7188	1.7281
0.2	22	0.5	0.5	0.5	1.0	1.7101	1.7149
0.2	23	0.5	0.5	0.5	1.0	1.6547	1.6524
0.2	21	1.0	0.5	0.5	1.0	1.2883	1.3818
0.2	21	1.5	0.5	0.5	1.0	1.0328	0.9861
0.2	21	0.5	1.0	0.5	1.0	1.4073	1.3131
0.2	21	0.5	1.5	0.5	1.0	0.8017	0.8489
0.2	21	0.5	0.5	1.0	1.0	1.5015	1.5575
0.2	21	0.5	0.5	1.5	1.0	1.3655	1.3376
0.2	21	0.5	0.5	0.5	1.1	1.7244	1.7724
0.2	21	0.5	0.5	0.5	1.2	1.7913	1.7674

Table 8. MLR Data for Sherwood number

β	Nb	Nt	Le	A	True Values	Predicted Values
0.2	0.5	0.5	0.5	1.0	0.6532	0.6922
0.3	0.5	0.5	0.5	1.0	0.6264	0.6408
0.4	0.5	0.5	0.5	1.0	0.5967	0.5895
0.2	1.0	0.5	0.5	1.0	0.9457	0.8804
0.2	1.5	0.5	0.5	1.0	1.0359	1.0686
0.2	0.5	0.7	0.5	1.0	0.5018	0.5156
0.2	0.5	1.1	0.5	1.0	0.1670	0.1624
0.2	0.5	0.5	1.0	1.0	1.0927	1.0331
0.2	0.5	0.5	1.5	1.0	1.3442	1.3740
0.2	0.5	0.5	0.5	1.1	0.7039	0.7181
0.2	0.5	0.5	0.5	1.2	0.7511	0.7440

Table 9. MLR Statistics for Skin Friction C_{f_x}, Nusselt Number N_{u_x}, Sherwood Number S_{h_x}

MLR Statistics	C_{f_x}	N_{u_x}	S_{h_x}
SE	0.001990	0.020025	0.014774
R-square	0.997	0.974	0.988
Observations	19	13	11
Adjusted R Square	0.996	0.948	0.977
RMSE	0.00869	0.07220	0.04900

Table 10. True and Predicted Values of Skin Friction Validation

Other Parameter Values	Ha	True Values of C_{f_x}	Predicted Values of C_{f_x}
$\beta = 0.2, \lambda = 0.1, We = 0.5, \beta^* = 0.2,$ A=1.0, $Pr = 21, Nt = 0.5, Nb = 0.5, Rd = 0.5, Le = 0.5$	0.5	1.1261	1.1212
	1.0	1.2587	1.2548
	1.5	1.3974	1.3883
	2.0	1.5146	1.5219

TABLE 11. True and Predicted Values of Nusselt Number Validation

Other Parameter Values	Pr	True Values of N_{u_x}	Predicted Values of N_{u_x}
	21	1.8220	1.7774
$\beta = 0.2, \lambda = 0.1, We = 0.5, \beta^* = 0.5,$	22	1.7101	1.7149
$Ha = 0.5, A = 1.0, Nt = 0.5, Nb = 0.5, Rd = 0.5, Le = 0.5$	23	1.6547	1.6524
	24	1.3634	1.5899
	25	1.3217	1.5273

TABLE 12. True and Predicted Values of Sherwood Number Validation

Other Parameter Values	Le	True Values of S_{h_x}	Predicted Values of S_{h_x}
	0.5	0.6532	0.6922
$\beta = 0.2, \lambda = 0.1, We = 0.5, \beta^* = 0.2,$	1.0	1.0927	1.0331
$Ha = 0.5, A = 1.0, Pr = 21, Nt = 0.5, Nb = 0.5, Rd = 0.5$	1.5	1.3442	1.3740

- Higher thermophoresis diffusion, Brownian motion, and radiation parameter values show that the temperature of the blood circulation maximized for boosting heat transfer and heat creation in the fluid.
- An increase in the Prandtl number might lower blood flow temperature due to an increased heat transfer rate and a lessened thermal diffusivity, leading to reduced heat accumulation and improving heat dissipation in the fluid.
- The unsteadiness parameter and Lewis number values are enhanced when the quantity of blood fluid lowers levels of the concentration gradient and a thinner concentration boundary layer.
- The machine learning methodology using multiple regression approaches produced outstanding results for predicting the behavior of MHD Williamson blood fluid flow passing through a wedge for the presented datasets. The most effective MLR is fitted in every situation of R^2 values close to 1 and provides 95% accuracy for showed and existent results.
- To validate the accuracy level of anticipated and numerical values for implementing the appropriate simple linear regression model.
- The outcomes of this research endeavor will be helpful to the researchers in evaluating the implications of velocity, temperature, and concentration on the physical attributes of MHD Williamson fluid, and cancer therapy for improved therapeutic regions are two potential benefits.
- Future studies could incorporate Williamson fluid, thermal energy radiation, and blood flow to assess efficacy and improve forecasting abilities. It could look into several methods for predicting the algorithm for K-mean approaches to clustering and artificially created neural network structures in the future.

6. Nomenclature

We - Weissenberg number $\left(We = \sqrt{\frac{\Gamma^2(m+1)u_e^3}{2\nu x}}\right)$
λ - Wedge moving parameter $\left(\lambda = \frac{b}{a}\right)$
Ha - Hartmann Number $\left(Ha^2 = \frac{\rho B_0^2}{ax^{m-1}}\right)$
A - Unsteadiness parameter $\left(A = \frac{c}{ax^{m-1}}\right)$
Pr - Prandtl number $\left(Pr = \frac{\mu C_P}{k}\right)$
α - Effective thermal diffusivity $\left(\alpha = \frac{k}{\rho C_P}\right)$
β - Wedge angle parameter $\left(\beta = \frac{2m}{m+1}\right)$
R_{e_x} - Local Reynolds number$\left(Re_x = \frac{xu_e(x)}{\nu}\right)$
Nt - Thermophoresis diffusion $\left(Nt = \frac{\tau D_T(T_w - T_\infty)}{T_\infty \nu}\right)$
Nb - Brownian motion $\left(Nb = \frac{\tau D_B(C_w - C_\infty)}{\nu}\right)$
β^* - Ratio of viscosity $\left(\beta^* = \frac{\mu_0}{\mu_\infty}\right)$
Rd - Radiation Parameter $\left(Rd = \frac{4\sigma^* T_\infty 3}{kk_1^*}\right)$
Le - Lewis number $\left(Le = \frac{\nu}{D_B}\right)$
B - Magnetic field $\left(\frac{kg}{S^2 A}\right)$
B_0 - Magnetic field strength $\left(\frac{A}{m}\right)$
σ - Electrical conductivity$\left(\frac{S}{m}\right)$
ρ - Fluid density $\left(\frac{kg}{m^3}\right)$
C_∞ - Ambient concentration
C_w - Concentration at the surface $\left(C_w(x,t) = C_\infty + \frac{C_0 x u_w}{\nu\sqrt{(1-ct)}}\right)$
C_0 - Initial reference concentration
C_P - Specific heat $\left(\frac{J}{kgK}\right)$
γ - Shear rate
ν - Kinematic coefficient of viscosity $\left(\frac{m^2}{S}\right)$
ψ - Stream function$(m^2 S)$
M - Stretching Parameter $\left(\frac{1}{S}\right)$
D_B - Brownian diffusion coefficient $\left(\frac{m^2}{S}\right)$
D_T - Thermophoresis diffusion coefficient $\left(\frac{m^2}{S}\right)$
μ_0 - Zero shear viscosity $\left(\frac{NS}{m^2}\right)$
μ_∞ - Infinite shear viscosity $\left(\frac{NS}{m^2}\right)$
f - Dimensionless stream function
θ - Dimensionless Temperature
ϕ - Dimensionless Concentration
σ^* - Stefan Boltzmann constant $\left(\frac{W}{m^2 K^4}\right)$
k^* - Rosseland mean absorption coefficient $\left(\frac{1}{m}\right)$

Γ - Material constants
q_s - Wall mass flux $\left(\frac{kg}{m^2 S}\right)$
q_r - radiative heat flux $\left(\frac{W}{m^2}\right)$
q_w - Wall heat flux $\left(\frac{W}{m^2}\right)$
Ω - Total Wedge angle
k - Thermal conductivity $\left(\frac{W}{mK}\right)$
τ_w - Wall shear stress $\left(\frac{N}{m^2}\right)$
T - Temperature(K)
T_0 - Initial reference temperature
T_w - Temperature at the surface $\left(T_w(x,t) = T_\infty + \frac{T_0 x u_w}{\nu\sqrt{(1-ct)}}\right)$
T_∞ - Ambient temperature
u - Velocity component along x direction$\left(\frac{m}{S}\right)$
v - Velocity component along y direction$\left(\frac{m}{S}\right)$
u_w - Stretching sheet velocity$\left(u_w(x,t) = \frac{bx^m}{1-ct}\right)$
u_e - Free stream velocity$\left(u_e(x,t) = \frac{ax^m}{1-ct}\right)$

References

1. Inoue S, Kabaya M, Biological activities caused by far-infrared radiation, *Int J Biometeorol 33:145–150,* ***1989.*** https://doi.org/10.1007/BF01084598
2. Kobu Y, Effects of infrared radiation on intraosseous blood flow and oxygen tension in rat tibia, *Kobe J Med Sci 45:27–39,* ***1999.*** https://pubmed.ncbi.nlm.nih.gov/10487033
3. Nishimoto C, Ishiura Y, Kuniasu K, Koga T, Effects of ultrasonic radiation on cutaneous blood flow in the paw of decerebrated rats, *Kawasaki J. Med Welfare 12:13–18,* ***2006.*** https://api.semanticscholar.org/CorpusID:70788743
4. Misra JC, Sinha A, Shit GC, Flow of a biomagnetic viscoelastic fluid: application to estimation of blood flow in arteries during electromagnetic hyperthermia, a therapeutic procedure for cancer treatment, *Appl Math Mech Eng Educ. 31:1405–1420,* ***2010.***https://doi.org/10.1007/s10483-010-1371-6
5. Mandal PK, An unsteady analysis of non-Newtonian blood flow through tapered arteries with a stenosis, *Int J nonlinear Mech, 40:51–164* ***2005***.https://doi.org/10.1016/j.ijnonlinmec.2004.07.007
6. Valencia A, Villanueva M, Unsteady flow and mass transfer in models of stenotic arteries considering fluid-structure interaction, *Int Comm Heat Mass Transfer, 33:966–75* ***2006***.https://doi.org/10.1016/j.icheatmasstransfer.2006.05.006
7. Bali R, Awasthi U, Effect of a magnetic field on the resistance to blood flow through the stenotic artery, *Applied Mathematics and Computation,188, 1635–1641* ***2007***. https://doi.org/10.1016/j.amc.2006.11.019
8. Habibi M R, Ghasemi M, Numerical study of magnetic nano-particles concentration in biofluid (blood) under the influence of high gradient magnetic field, *Journal of Magnetism and Magnetic Materials 323, 32–38,* ***2011***.https://doi.org/10.1016/j.jmmm.2010.08.023
9. Akbar N S, Nadeem S, Lee C, Influence of heat transfer and chemical reactions on Williamson fluid model for blood flow through a tapered artery with a stenosis, *Asian J. Chem. 24 (6), 2433e2441,* ***2012***.https://doi.org/10.1615/HeatTransRes.2012004295
10. Reddy S R R, Reddy P B A, Suneetha S, Magnetohydrodynamic flow of blood in a permeable inclined stretching viscous dissipation, non-uniform heat source/sink and chemical reaction, *Front. Heat Mass Transf. 10 (22)* ***2018.***https://doi.org/10.5098/HMT.10.22

11. Falkner VM, Skan SW, Some approximate solutions of the boundary-layer for flow past a stretching boundary, *SIAM J Appl Math, 46:1350–8,* ***1931***. http://dx.doi.org/10.1080/14786443109461870
12. Kuo BL, Application of the differential transformation method to the solutions of Falkner-Skan wedge flow, *Acta Mech, 164:161–74* ***2003***. https://doi.org/10.1007/s00707-003-0019-4
13. Chamkha AJ, Mujtaba M, Quadri A, Issa C, Thermal radiation effects on MHD forced convection flow adjacent to a non-isothermal wedge in the presence of heat source or sink, *Heat Mass Transf, 39:305–12,* ***2003***.https://doi.org/10.1007/S00231-002-0353-4
14. Hsiao KL, MHD mixed convection for viscoelastic fluid past a porous wedge, *Int J Eng Sci, 46:1–8,* ***2011***. https://doi.org/10.1016/j.ijnonlinmec.2010.06.005
15. Alam MS, Islam T, Rahman MM, Unsteady hydromagnetic forced convective heat transfer flow of a micropolar fluid along a porous wedge with convective surface boundary condition, *Int J Heat Tech, 33,* ***2015***. https://doi.org/10.18280/IJHT.330219
16. Williamson R V, The flow of pseudo-plastic materials, *Ind. Eng. Chem. 21 (11),* ***1929***. https://doi.org/10.1021/ie50239a035
17. Sreenadh S, Goverdhan P, Ravi Kumar Y V K, Effect of slip and heat transfer on the Peristaltic pumping of a Williamson fluid in an inclined channel, *Int. J. Appl. Sci. Eng. 12 (2), pp 143–155,* ***2014***. https://doi.org/10.6703/IJASE.2014.12(2).143
18. Raju C S, Sandeep N, Ali M E, Nuhait A O, Heat and mass transfer in 3-d MHD Williamson-Casson fluids flow over a stretching surface with non-uniform heat source/sink, *Thermal Science 23 (1), 281–293,* ***2019***. https://doi.org/10.2298/TSCI160426107R
19. Kumaran G, Sandeep N, Thermophoresis and Brownian moment effects on the parabolic flow of MHD Casson and Williamson fluids with cross-diffusion, *J. Mol. Liq. 233* ***2017.*** https://doi.org/10.1016/j.molliq.2017.03.031
20. Makinde O D, Mabood F, Ibrahim M S, Chemically reacting on MHD boundary-layer flow of nanofluids over a nonlinear stretching sheet with heat source/sink and thermal radiation, *Therm. Sci. 22 (1B)* ***2018***. https://doi.org/10.2298/TSCI151003284M
21. Amanulla C H, Nagendra N, Reddy M S, Numerical simulation of slip influence on the flow of an MHD Williamson fluid over a vertical convective surface, *Nonlin. Eng. 7 (4)* ***2018.*** https://doi.org/10.1515/nleng-2017-0079
22. Ahmed K, Akbar T, Numerical investigation of magnetohydrodynamics Williamson nanofluid flow over an exponentially stretching surface, *Adv. Mech. Eng. 13* ***2021.*** https://doi.org/10.1177/16878140211019875
23. Wakif A, A novel numerical procedure for simulating steady MHD convective flows of radiative Casson fluids over a horizontal stretching sheet with irregular geometry under the combined influence of temperature-dependent viscosity and thermal conductivity, *Mathematical Problems in Engineering, Article ID 1675350, 20 pages,* ***2020.*** https://doi.org/10.1155/2020/1675350
24. Tuz Zohra F, Uddin M J, Basir M F, and Ismail A I M, Magnetohydrodynamic bio-nano-convective slip flow with Stefan blowing effects over a rotating disc, *Proc. Inst. Mech. Eng. N 234, 83–97* ***2020.*** https://doi.org/10.1177/2397791419881580
25. Basha H T, Sivaraj R, Numerical simulation of blood nanofluid flow over three different geometries using gyrotactic microorganisms: applications to the flow in a circulatory system, *Proc. Instit. Mech. Eng., Part C: J. Mech. Eng. Sci. 235 (2) 441–460* ***2021***. https://doi.org/10.1177/0954406220947454
26. Kuo B L, Application of the differential transformation method to the solutions of Falkner-Skan wedge flow, *Acta Mech. 164, 161e174,* ***2003***. https://link.springer.com/article/10.1007/s00707-003-0019-4
27. Ishaq A, Nazar R, Pop I, Moving wedge and flat plate in a micropolar fluid, *Intermt. J. Sci. 44 1225e1236,* ***2006***. https://doi.org/10.1016/j.ijengsci.2006.08.005

28. Hamid A, Hashim, Khan M, Numerical investigation on heat transfer performance in time-dependent flow of Williamson fluid past a wedge-shaped geometry, *Results Phys. 9, 479e485* ***2018***. http://dx.doi.org/10.1016/j.rinp.2018.01.025
29. Subbarayudu K, Suneetha S, Bala Anki Reddy P, The assessment of the time-dependent flow of Williamson fluid with radiative blood flow against a wedge, *Propul. Power Res. 9 (1), 87–99* ***2020***. http://dx.doi.org/10.1016/j.jppr.2019.07.001
30. Khan M, Malik M Y, Salahuddin T, Hussian A, Heat and mass transfer of Williamson nanofluid flow yield by an inclined Lorentz force over a nonlinear stretching sheet, *Results Phys. 8* ***2018.*** https://doi.org/10.1016/j.rinp.2018.01.005
31. Khan M, Hamid A, Influence of nonlinear thermal radiation on the 2D unsteady flow of a Williamson fluid with heat source/sink, *Results Phys. 7 3968e3975,* ***2017***. https://doi.org/10.1016/j.rinp.2017.10.014
32. Khan W A, Gorla R S R, Heat and mass transfer in non-Newtonian nanofluids over a non-isothermal stretching wall, *J. Nanoeng. Nano Syst. 225 (4), 155e163* ***2012***. https://doi.org/10.1177/1740349912440680
33. Alam M S, Islam T, Rahman M M, Unsteady hydromagnetic forced convective heat transfer flow of a micropolar fluid along a porous wedge with convective surface boundary condition, *Int. J. Heat Tech. 33* ***2015***. http://dx.doi.org/10.18280/ijht.330219
34. Shampine L F, Gladwell I, Thompson S, Solving ODEs with Matlab, *Cambridge University Press,* ***2003***. https://doi.org/10.1017/CBO9780511615542
35. Shampine L F, Kierzenka J, Reichelt M W, Solving boundary value problems for ordinary differential equations in MATLAB with bvp4c, *Tutorial Notes, 1–27,* ***2000***. https://api.semanticscholar.org/CorpusID:427544
36. Umair K, Aurang Z, Sakhinah A B, Anuar I, Dumitru B, Sayed E L Sherif M, computational simulation of cross-flow of Williamson fluid over a porous shrinking/stretching surface comprising hybrid nanofluid and thermal radiation. *AIMS Mathematics, 7(4): 6489–6515,* ***2022***. https://doi.org/10.3934/math.2022362
37. Chu Y M, Khan U, Shafiq A, Zaib A, Numerical simulations of time-dependent micro-rotation blood flow induced by a curved moving surface through conduction of gold particles with non-uniform heat sink/source, *Arab. J. Sci. Eng., 46, 2413–2427,* ***2021***. https://doi.org/10.1007/s13369-020-05106-0
38. Firuz Kamalov, Aswani Kumar Cherukuri, Hana Sulieman, Fadi Thabtah, Akbar Hossain, Chapter 17 - Machine learning applications for COVID-19: a state-of-the-art review, *Data Science for Genomics, 277-289,* ***2023***. https://doi.org/10.1016/B978-0-323-98352-5.00010-0
39. Firuz Kamalov, Khairan Rajab, Aswani Kumar Cherukuri, Ashraf Elnagar, Murodbek Safaraliev, Deep learning for Covid-19 forecasting: State-of-the-art review. *Neurocomputing, 511, 142-154,* ***2022***. https://doi.org/10.1016/j.neucom.2022.09.005
40. Palash S, Ramesh K, Parameshwaran R, Sandip S. Deshmukh, Thermal conductivity prediction of titania-water nanofluid: A case study using different machine learning algorithms, *Case Studies in Thermal Engineering, 30, 101658,* ***2022***. https://doi.org/10.1016/j.csite.2021.101658
41. Sulochana C, Kumar T, Regression modeling of hybrid nanofluid flow past an exponentially stretching/shrinking surface with heat source-sink effect, *Materials Today: Proceedings, 54,* ***2021***. https://doi.org/10.1016/j.matpr.2021.10.375
42. Priyadharshini P, Vanitha Archana M, Ameer Ahammad N, Raju C S K, Se-jin Yook, Nehad Ali Shah, Machine learning regression using gradient descent for MHD flow: Metallurgy process, *International Communications in Heat and Mass Transfer, 138, 106307,* ***2022***. https://doi.org/10.1016/j.icheatmasstransfer.2022.106307
43. Priyadharshini P, Vanitha Archana M, Augmentation of magnetohydrodynamic nanofluid flow through a Permeable stretching sheet employing Machine learning algorithm, *Examples and Counterexamples, 3, 100093,* ***2023***. https://doi.org/10.1016/j.exco.2022.100093

44. Dinesh Kumar M, Ameer Ahammad N, Raju C S K, Se-Jin Yook, Nehad Ali Shah, Sayed M, Response surface methodology optimization of dynamical solutions of Lie group analysis for nonlinear radiated magnetized unsteady wedge: Machine learning approach (gradient descent) *Alexandria Engineering Journal, 74, 29–50,**2023**.* https://doi.org/10.1016/j.aej.2023.05.009
45. Priyadharshini P, Karpagam V, Nehad Ali Shah, Mansoor H. Alshehri, Bio- Convection effects of MHD Williamson fluid flow over a symmetrically stretching sheet: Machine learning *MDPI Symmetry, 15(9), 1684, **2023**.* https://doi.org/10.3390/sym15091684
46. Misra J C, Sinha A, Effect of thermal radiation on MHD flow of blood and heat transfer in a Permeable capillary in stretching motion, *Heat Mass Transf. 49 617e628 **2013**.* https://doi.org/10.1007/s00231-012-1107-6
47. Valvano J W, Nho S, Anderson G T, Analysis of the Weinbaum-Jiji model of blood flow in the canine kidney cortex for self-heated thermistors, *J. Biomech. Eng. 116 201e207 **1999**.* https://doi.org/10.1115/1.2895720
48. Chato J C, Heat transfer to blood vessels, *J. Biomech. Eng. 102 110e118 **1980**.* https://doi.org/10.1115/1.3138205

[1,2] Department of Mathematics, PSG College of Arts and Science, Coimbatore-641014, Tamil Nadu, India.
Email address: priyadharshinip@psgcas.ac.in
Email address: karpagamdangae03@gmail.com